International Journal of Clinical Inventions and Medical Sciences
p-ISSN: 2721-4737, e-ISSN: 2721-7302

Original Research Report

Spectral Subtraction Denoising (SSD) Improves Factor-3 GRAPPA 3T Lumbar MRI for Disc Herniation

Ildsa Maulidya Mar'athus Nasokha[1*], Retno Wati[1], Mei Arnefia[1]

[1] *Program of Radiology, Faculty of Health Sciences, Universitas 'Aisyiyah Yogyakarta. Yogyakarta, Indonesia.*

Article History
Received:
08.06.2026

Revised:
12.07.2026

Accepted:
28.07.2026

***Corresponding Author:**
Ildsa Maulidya Mar'athus Nasokha
Email:
maulidya.ildsa@unisayogya.ac.id

Abstract: Parallel imaging shortens lumbar MRI examinations but factor-3 GRAPPA produces spatially varying noise that can obscure clinically important structures. Evidence for a simple, reproducible spectral subtraction denoising approach in clinically acquired 3T lumbar examinations remains limited. This paired pretest-posttest study evaluated MATLAB-based spectral subtraction denoising (SSD) in 16 patients with clinically diagnosed lumbar disc herniation. Sagittal T2-weighted TSE-GRAPPA images acquired at acceleration factor 3 were processed by estimating the background-noise spectrum, directly subtracting it from the image spectrum, retaining the original phase, and applying an inverse Fourier transform. Signal-to-noise ratio (SNR) was measured in five anatomical regions, and two radiologists with more than five years of experience independently performed blinded five-point visual grading. Paired differences were assessed with the Wilcoxon signed-rank test; acceleration-factor comparisons used the Friedman test, and interobserver agreement used Cohen's kappa. SSD increased SNR in every evaluated structure, with the largest absolute gains in the vertebral body (+1.81) and degenerated nucleus pulposus (+0.41). Overall visual information improved ($p < 0.001$); four of five structures improved significantly, whereas the vertebral body showed a ceiling effect ($p = 0.236$). Interobserver agreement increased from $\kappa = 0.60$ to $\kappa = 0.72$. The findings support SSD as a low-complexity post-processing option for preserving diagnostic visibility in accelerated lumbar MRI. Larger multicenter studies should compare SSD with modern learning-based denoisers and evaluate diagnostic accuracy.

Keywords: Computational Imaging, GRAPPA, Image Enhancement, Medical Image Processing, MRI Denoising.

International Journal of Clinical Inventions and Medical Sciences, vol. 8, no. 2, pp. 27-37, September 2026. **DOI: 10.36079/lamintang.ijcims-0802.1047**

1. Introduction

Low back pain is a major contributor to disability and frequently prompts lumbar imaging when persistent symptoms, neurologic deficits, or red-flag features are present [1] - [3]. Lumbar disc herniation is clinically important because displacement of disc material can narrow the spinal canal or neural foramina and compress neural structures. Standardized anatomical terminology and reliable visualization of the vertebral bodies, intervertebral discs, spinal canal, neural elements, and degenerated nucleus pulposus are therefore central to radiological interpretation [4] - [6].

Magnetic resonance imaging (MRI) is the preferred cross-sectional modality for evaluating disc and neural soft tissues because it provides strong tissue contrast without ionizing radiation [3]. The practical limitation is acquisition time. Patients with acute pain may have difficulty remaining still, and long protocols reduce scanner throughput. Parallel imaging methods such as sensitivity encoding and generalized autocalibrating partially parallel acquisitions (GRAPPA) shorten acquisition by undersampling phase-encoding lines and using the spatial sensitivity of multichannel receiver coils to reconstruct missing data [7] - [10]. The time saving is accompanied by a predictable SNR penalty and a spatially nonuniform geometry-factor noise pattern, particularly at higher acceleration factors.

Prior spine studies have shown that moderate parallel acceleration can preserve diagnostic utility while reducing examination time [11] - [13]. However, the residual noise is not uniform across the field of view and may disproportionately affect low-signal structures, disc margins, and boundaries adjacent to cerebrospinal fluid. Conventional smoothing can suppress noise but may also blur the high-frequency edges required to evaluate disc protrusion and canal compromise. This creates a computational problem: the post-processing method should reduce spatial noise without erasing anatomically meaningful boundaries.

Spectral subtraction denoising (SSD) estimates a noise spectrum from signal-free data and subtracts that estimate from the measured magnitude spectrum before image reconstruction [14] - [16]. It is computationally light because it requires one forward and one inverse Fourier transform, and it does not require a training dataset. A previous investigation by the present research group evaluated SSD across GRAPPA acceleration factors in lumbar MRI [17]. Nevertheless, the clinically relevant factor-3 condition, the anatomy-specific pattern of improvement, the reproducible processing formulation, and its relationship to blinded visual grading were not sufficiently reported.

This study therefore evaluates direct frequency-domain SSD for factor-3 GRAPPA sagittal T2-weighted 3T lumbar MRI in patients with disc herniation. The novelty is not a claim that spectral subtraction itself is new; rather, it is a paired, anatomy-specific computational evaluation of a low-complexity method under a clinically meaningful acceleration setting. The objectives were to quantify SNR changes in five anatomical regions, determine whether radiologists perceived improved structural visibility, assess interobserver agreement, and explain why the magnitude of improvement differed among structures. The study contributes a reproducible formulation, pseudocode, an integrated quantitative-qualitative evaluation framework, and clinically bounded conclusions.

2. Literature Review

2.1. Parallel Imaging and Spatially Varying Noise

GRAPPA reconstructs missing k-space lines by learning interpolation weights from autocalibration data and combining information from multiple receiver coils [7] [9]. If the acceleration factor is R, the ideal SNR loss includes a factor proportional to $1/\sqrt{R}$, with additional spatially dependent degradation represented by the geometry factor [9] [10]. As a result, two pixels with similar native tissue signal can exhibit different uncertainty after reconstruction. In lumbar imaging, this matters because the vertebral marrow, low-signal degenerated discs, the spinal canal, and neural tissues occupy different positions relative to coil sensitivity profiles.

Clinical studies of lumbar and cervical spine MRI have demonstrated that acceleration can substantially reduce scan time while retaining acceptable interpretation, but the optimal factor depends on field strength, coil geometry, sequence, and the anatomical task [11] [12]. Compressed sensing and deep learning reconstruction can extend acceleration further, although these methods introduce additional reconstruction assumptions and software dependencies [13] [20] - [28]. A simple post-reconstruction method remains relevant where raw-data access, large training sets, or vendor-specific deep learning tools are unavailable.

2.2. MRI Noise and Spectral Subtraction

Thermal noise in complex MR data is commonly approximated as Gaussian. After magnitude reconstruction, the distribution becomes Rician in single-coil data and can be more complex after multicoil combination and parallel reconstruction [14] [15]. This distinction is important at low SNR because the magnitude operation introduces a positive bias. Spatially varying noise also limits the validity of an SNR estimate that uses only one remote background region. For paired images from the same acquisition, however, consistent ROI placement can still provide a practical within-subject comparison when its limitations are acknowledged.

SSD was originally developed for additive noise removal in the spectral domain. In MRI, the measured spectrum is treated as the sum of the true signal spectrum and a background-noise spectrum. The noise magnitude estimate is subtracted, nonphysical negative magnitudes are clipped, and the original phase is retained before the inverse transform [16]. Compared with broad low-pass smoothing, spectral subtraction is intended to preserve high-frequency phase and edge information. Its principal risk is over-subtraction, which can create spectral holes or remove weak tissue signal; therefore, anatomical validation is necessary.

2.3. Quantitative and Visual Image-Quality Assessment

SNR and contrast-to-noise ratio are widely used to evaluate MRI acquisition and reconstruction, but partially parallel imaging requires careful interpretation because noise is spatially correlated and nonstationary [10] [29]. Quantitative metrics should therefore be paired with an observer-based assessment of the structures relevant to the clinical task. Visual grading analysis uses predefined anatomical criteria and ordinal scores, and nonparametric statistics are appropriate for paired ordinal ratings [30]. Cohen's kappa complements the grading comparison by describing agreement beyond chance [31] [32].

2.4. Research Gap and Conceptual Framework

Recent learning-based reconstruction studies have reported substantial scan-time reductions and improved perceived image quality in lumbar MRI [20] - [28]. Their performance, however, depends on training data, scanner integration, and external validation. The present study addresses a narrower but practical gap: whether direct SSD can recover anatomy-specific visibility from clinically acquired factor-3 GRAPPA images using a transparent algorithm that can be implemented in a standard numerical environment. The conceptual framework links GRAPPA-related undersampling noise to spectral estimation, paired denoising, objective ROI measurement, and blinded clinical grading.

3. Methodology

3.1. Study Design and Setting

A pre-experimental one-group pretest-posttest design was used. Data were acquired at the Radiology Department of RSUD Dr. Soedono Madiun, Indonesia, from January to February 2020. Each patient served as their own control: the factor-3 image was evaluated before SSD and again after SSD. The broader source protocol acquired acceleration factors 2, 3, and 4; factor 3 was selected for the primary paired analysis because it provided the most favorable balance between examination time and retained visual information.

3.2. Participants, Sampling, and Sample-Size Justification

The sample-size calculation for one paired numerical group used a two-sided α of 0.05, 80% power, and a large standardized effect size of 0.80. The minimum calculated sample was 14; 16 patients were enrolled to allow for possible attrition. A hospital-based eligibility approach was used: eligible and consenting patients encountered during the study window were enrolled until the planned sample was reached. Inclusion required a clinical diagnosis of lumbar disc herniation and referral for lumbar MRI. Patients without that clinical diagnosis and patients unwilling to participate were excluded. The image archive contained 16 complete examinations. Age and sex were recorded during routine acquisition, but an analyzable de-identified demographic summary was not retained in the archived research dataset; no demographic values were inferred.

Two consultant radiologists, each with more than five years of MRI interpretation experience, served as observers. Before scoring, the assessment criteria and anatomical landmarks were reviewed

jointly using images that were not included in the scored dataset. The observers then rated independently and were blinded to patient identity, acceleration parameters, and processing condition.

Table 1. Study, Acquisition, and Processing Characteristics

Characteristic	Specification
Design	Paired one-group pretest-posttest
Setting and period	RSUD Dr. Soedono Madiun; January–February 2020
Participants	16 patients with clinically diagnosed lumbar disc herniation
Sample-size basis	Minimum 14; α = 0.05, power = 0.80, effect size = 0.80; enrolled n = 16
Scanner / sequence	3T MRI; sagittal T2-weighted TSE-GRAPPA
Acceleration factors acquired	2, 3, and 4; primary paired analysis at factor 3
Fixed acquisition parameters	TR 3800 ms; TE 110 ms; slice thickness 4 mm; FOV 300 × 300 mm
Factor-3 scan time	1 min 48 s (factor 2: 2 min 34 s; factor 4: 1 min 25 s)
Observers	Two radiologists, each >5 years of experience
Software	MATLAB-based archived workflow; exact release not retained
Primary outcomes	ROI-based SNR and blinded five-point visual grading

3.3. MRI Acquisition and Image Selection

Patients were positioned supine using the routine lumbar-spine coil configuration. The sagittal T2-weighted TSE-GRAPPA sequence was acquired with repetition time 3800 ms, echo time 110 ms, slice thickness 4 mm, and field of view 300 × 300 mm. The routine factor-2 sequence was copied and the acceleration setting was changed to factors 3 and 4 while the listed parameters were held constant. The corresponding scan times were 2 min 34 s, 1 min 48 s, and 1 min 25 s. Thus, factor 3 reduced acquisition time by approximately 36.8% relative to factor 2 while avoiding the stronger image-quality penalty observed at factor 4.

3.4. Spectral Subtraction Formulation and Implementation

Let $y(x,y)$ denote the baseline reconstructed image and Y(u,v) its two-dimensional Fourier transform. The measured spectrum was modeled as the sum of the anatomical signal spectrum S(u,v) and noise spectrum N(u,v):

$$Y(u,v) = S(u,v) + N(u,v) \quad (1)$$

A signal-free background region was used to estimate the mean noise magnitude spectrum $|\hat{N}(u,v)|$. The archived implementation used direct magnitude subtraction, equivalent to an over-subtraction factor α = 1 and no additional spectral floor (β = 0). Negative magnitudes were clipped to zero:

$$|\hat{S}(u,v)| = max(|Y(u,v)| - |\hat{N}(u,v)|, 0) \quad (2)$$

The phase of the measured spectrum was retained, and the denoised image was reconstructed by inverse Fourier transformation:

$$\hat{s}(x,y) = F^{-1}\{|\hat{S}(u,v)| \exp[j\angle Y(u,v)]\} \quad (3)$$

International Journal of Clinical Inventions and Medical Sciences, vol. 8, no. 2, pp. 27-37, September 2026. **DOI: 10.36079/lamintang.ijcims-0802.1047**

The exact MATLAB release was not preserved in the archived protocol; the operations in Equations (1), (2)) and (3) are version-independent. The explicit formulation and pseudocode below replace the previously vague software description and enable implementation in MATLAB, Python, or another numerical environment.

Input: baseline magnitude image I and signal-free background mask B

1 Normalize I to floating-point intensity.
2 Compute Y = fftshift(fft2(I)).
3 Estimate the mean background-noise magnitude spectrum N from B.
4 Compute M = max(abs(Y) − N, 0).
5 Recombine M with phase(Y): Yd = M · exp(j·angle(Y)).
6 Compute Id = real(ifft2(ifftshift(Yd))).
7 Restore the original display range and export the denoised DICOM image.

Output: denoised image Id.

Algorithm 1. Direct Spectral Subtraction Denoising

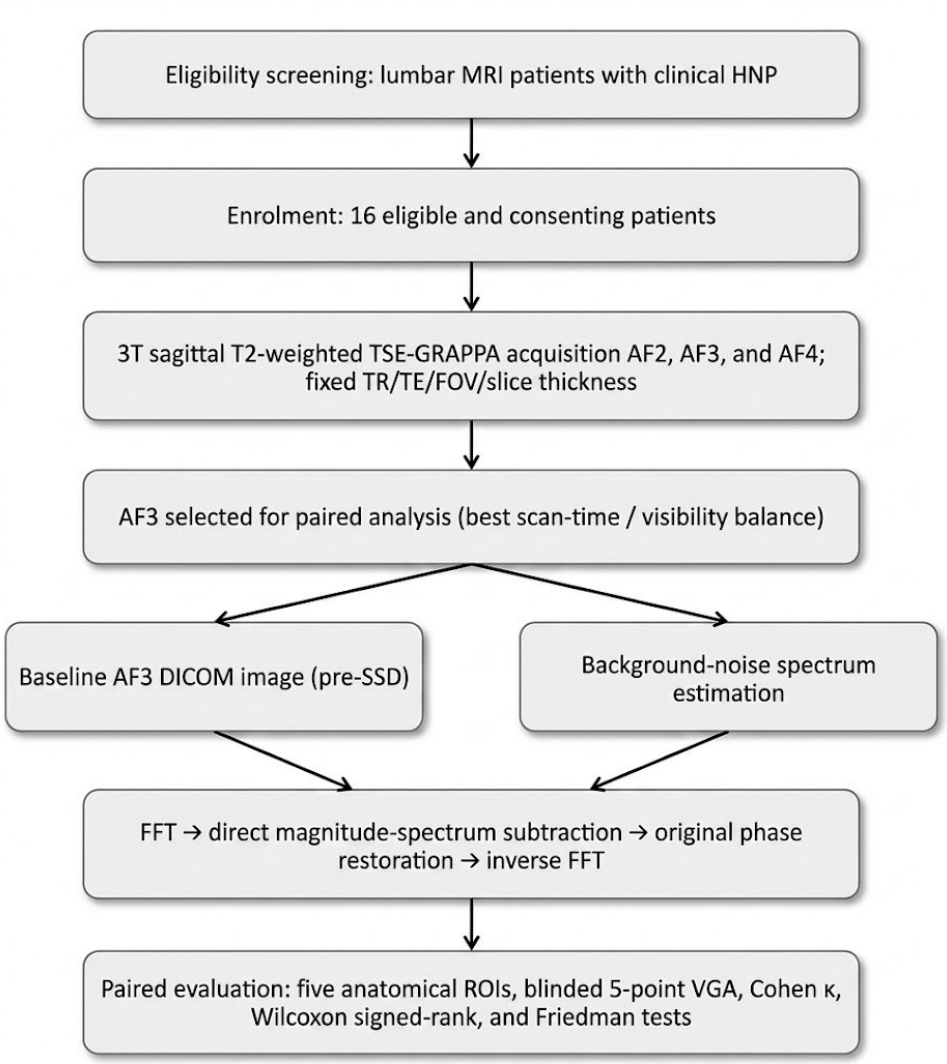

Figure 1. End-to-End Acquisition, SSD Processing, and Evaluation Workflow

3.5. ROI Measurement and Visual Grading

SNR was calculated for five prespecified anatomical regions: vertebral body, spinal cord, degenerated nucleus pulposus, spinal canal, and intervertebral disc. For each patient, an anatomical ROI and a signal-free background ROI were placed on the baseline image; the coordinates and areas were copied to the paired post-SSD image so that the comparison was not confounded by different sampling locations. The same slice level was used within each pair. Because parallel-imaging noise is spatially nonstationary, the resulting SNR values are interpreted as paired practical indices rather than absolute physical SNR measurements [10] [29].

For qualitative assessment, the observers independently evaluated the visibility of the same five structures on anonymized, randomly coded images. The original five-level scale was retained: 1 = very good (clear, readily visible, and no clinical limitation), 2 = good, 3 = adequate, 4 = limited, and 5 = poor. Lower scores therefore indicated better visibility. Each condition generated 80 anatomical ratings (16 patients × 5 structures) per observer.

3.6. Statistical Analysis

Normality was screened with the Shapiro-Wilk test. Because the visual scores were paired and ordinal, the Wilcoxon signed-rank test compared factor-3 images before and after SSD. The Friedman test was used for comparisons across acceleration factors 2, 3, and 4. Cohen's kappa quantified interobserver agreement. A two-sided p value below 0.05 was considered statistically significant. The terms moderate and substantial agreement follow conventional kappa interpretation while recognizing that kappa depends on prevalence and category distribution [31] [32].

3.7. Ethical Considerations

The study received permission from the Health Research Ethics Committee of RSUD Dr. Soedono Madiun with ethics committee issued an approval number No.070/116125/303/2020. Participation was voluntary, and images were coded before observer assessment. The archived study documents did not preserve the approval identifier; consequently, no identifier has been invented in this revision.

4. Finding and Discussion

4.1. Quantitative findings

SSD increased the paired SNR index in all five anatomical regions (Table 2). The vertebral body showed the largest absolute increase, from 5.61 to 7.42 (+1.81; 32.3%). The degenerated nucleus pulposus increased from 1.18 to 1.59 (+0.41; 34.7%). The intervertebral disc had the largest relative increase (50.0%), but its absolute change was small because the baseline signal was low. The spinal cord and spinal canal showed smaller numerical gains of 0.17 and 0.16, respectively.

Table 2. Anatomy-Specific SNR Before and After SSD at Acceleration Factor 3

Anatomical Region	Before SSD	After SSD	Absolute Change	Relative Change
Vertebral body	5.61	7.42	+1.81	+32.3%
Spinal cord	3.98	4.15	+0.17	+4.3%
Degenerated nucleus pulposus	1.18	1.59	+0.41	+34.7%
Spinal canal	2.92	3.08	+0.16	+5.5%
Intervertebral disc	0.22	0.33	+0.11	+50.0%

The source experiment also reported no statistically significant difference in spatial resolution across acceleration conditions ($p = 0.21$). This supports the interpretation that the observed changes were predominantly related to noise suppression rather than an acquisition-driven change in nominal spatial resolution.

4.2. Visual Grading and Observer Agreement

Overall anatomical visibility improved after SSD ($p < 0.001$). Four of the five structures showed significant paired improvement: spinal cord ($p < 0.001$), degenerated nucleus pulposus ($p = 0.002$), spinal canal ($p < 0.001$), and intervertebral disc ($p < 0.001$). The vertebral body did not show a statistically significant visual change ($p = 0.236$), despite its large SNR increase. Interobserver agreement increased from $\kappa = 0.60$ before SSD to $\kappa = 0.72$ after SSD, indicating a transition from the upper boundary of moderate agreement to substantial agreement.

Table 3. Visual Grading and Interobserver Results at Acceleration Factor 3

Outcome	Before SSD	After SSD / Paired Result	Interpretation
Overall anatomical visibility	—	$p < 0.001$	Significant improvement
Vertebral body	—	$p = 0.236$	No significant visual change
Spinal cord	—	$p < 0.001$	Significant improvement
Degenerated nucleus pulposus	—	$p = 0.002$	Significant improvement
Spinal canal	—	$p < 0.001$	Significant improvement
Intervertebral disc	—	$p < 0.001$	Significant improvement
Interobserver agreement	$\kappa = 0.60$	$\kappa = 0.72$	Moderate to substantial

Figure 2 shows representative factor-3 sagittal T2-weighted images before and after SSD. Arrows identify the principal anatomical regions used for quantitative and visual assessment. The panels are illustrative source images and are not pixel registered.

4.3. Mechanistic Interpretation of Anatomy-Specific Effects

The anatomy-specific pattern clarifies why a single global statement that "SSD improves image quality" is insufficient. The vertebral body contains a relatively broad and homogeneous marrow region. Averaging over this region can produce a large numerical SNR gain when background noise decreases, yet the structure may already be easy to see on the baseline image. The nonsignificant visual result is therefore consistent with a ceiling effect: radiologists had limited opportunity to assign a better category after denoising.

By contrast, the degenerated nucleus pulposus and intervertebral disc are low-signal structures whose interpretation depends on subtle differences in signal and the continuity of the annular and posterior disc margins. Suppressing broadband noise makes these boundaries more coherent, which explains why the visual improvement was significant even when the absolute SNR change was smaller than that of the vertebral body. The 50% relative disc increase should not be overinterpreted because it arose from a very low baseline value; the paired visual result provides the clinically relevant corroboration.

The spinal canal and spinal cord showed small numerical SNR increases but strong visual significance. These structures are adjacent to bright cerebrospinal fluid on T2-weighted imaging, so diagnostic visibility depends on boundary stability rather than only on mean signal intensity. Retaining the measured spectral phase while reducing noise magnitude can stabilize edges without applying broad spatial smoothing. This mechanism is consistent with the observed improvement in observer agreement.

4.4. Comparison with Previous Work

The findings agree with the original SSD MRI study, which reported meaningful SNR recovery with a low-complexity spectral-domain operation [16], and with the prior report from this dataset showing improved image quality across GRAPPA acceleration factors [17]. The present analysis strengthens that work by isolating the clinically relevant factor-3 condition, reporting paired anatomical regions,

International Journal of Clinical Inventions and Medical Sciences, vol. 8, no. 2, pp. 27-37, September 2026. **DOI: 10.36079/lamintang.ijcims-0802.1047**

distinguishing absolute from relative gains, and linking SNR changes to blinded structure-specific grading.

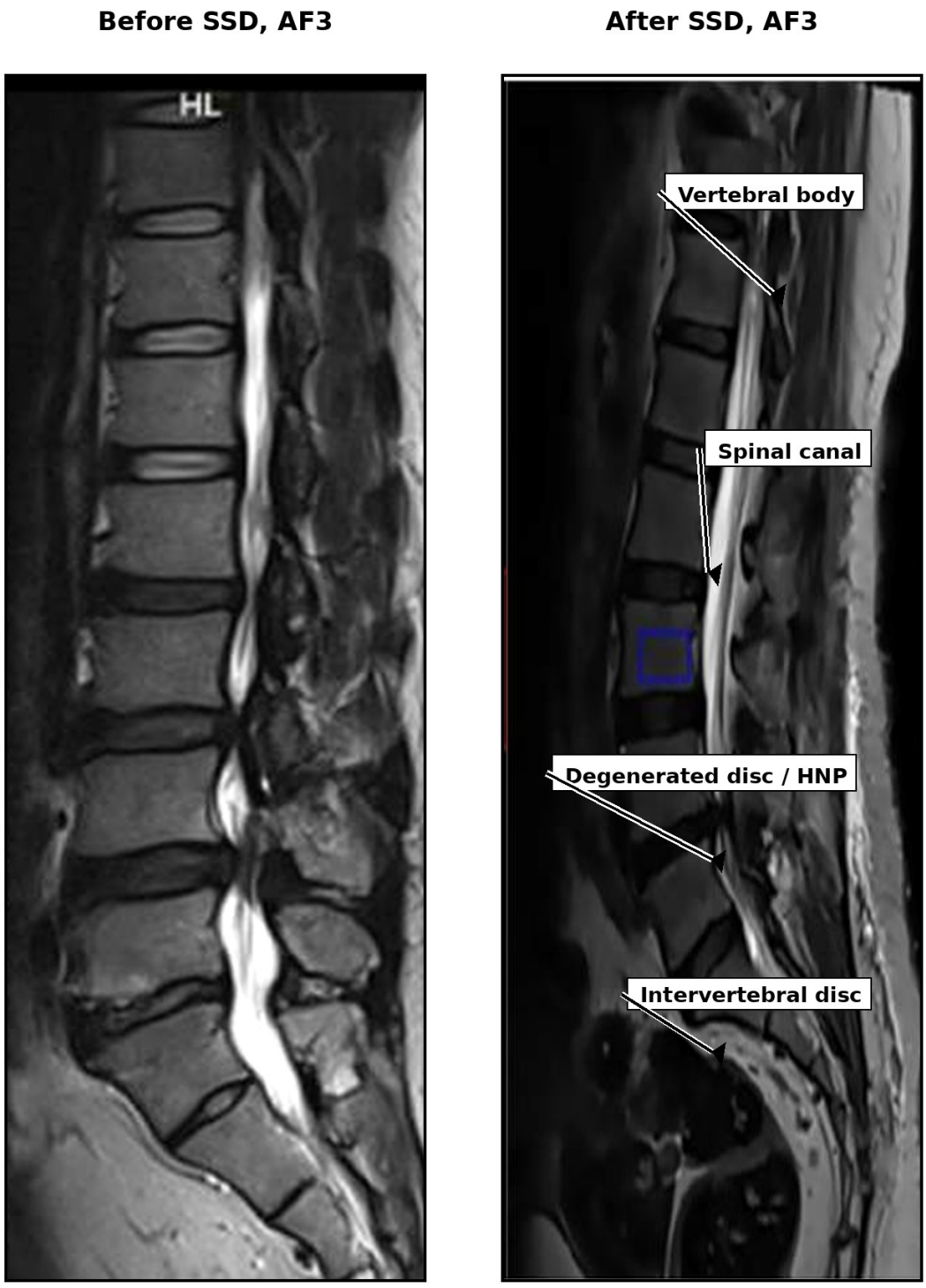

Figure 2. Comparison of Sagittal T2-Weighted Images (Pre vs Post-SSD)

Parallel-imaging studies in the spine have shown that moderate acceleration can preserve diagnostic utility, whereas stronger acceleration increases noise and nonuniformity [11] [12]. In this dataset, factor 3 shortened the sagittal sequence from 2 min 34 s to 1 min 48 s, a 36.8% reduction

relative to factor 2, while factor 4 was faster but visually less favorable. This supports factor 3 as a pragmatic operating point rather than a universal optimum.

Modern deep learning reconstruction studies report larger reductions in lumbar MRI time and frequently higher perceived image quality [20] - [28]. Those approaches are important comparators but do not make simple methods obsolete. SSD requires no training corpus, can be audited directly, and can be implemented outside a vendor-specific reconstruction stack. Its expected role is therefore complementary: a transparent baseline or a resource-efficient post-processing option, not a replacement for validated learning-based reconstruction.

4.5. Computational and Clinical Implications

From a computational perspective, the revised workflow exposes each operation and parameter, making the method reproducible and easy to test. The use of direct subtraction ($\alpha = 1$, $\beta = 0$) minimizes parameter tuning. This simplicity also provides a useful benchmark against which more complex denoisers can be evaluated. Future implementations should estimate spatially varying noise maps, test spectral floors that prevent over-subtraction, and report execution time and memory use.

Clinically, the results support improved visibility rather than proven diagnostic accuracy. The study did not test sensitivity, specificity, treatment decisions, or patient outcomes. The most defensible implication is that SSD may help radiologists evaluate disc and canal boundaries on accelerated factor-3 images and may reduce disagreement between observers. Any claim that it improves diagnosis should be tested prospectively against an independent reference standard.

4.6. Limitations

This study has several limitations. First, the sample was small (16 patients), single-center, and obtained from one scanner and one sagittal T2-weighted protocol. Second, demographic summary data were not retained in the analyzable archive, limiting assessment of sample representativeness. Third, ROI dimensions were not stored as a standardized pixel count, although paired coordinates and areas were maintained within each subject. Fourth, two observers were used and no external diagnostic reference standard was available. Finally, SSD was not directly compared with nonlocal means, compressed sensing, or deep learning denoisers. These limitations restrict generalization and preclude claims of improved diagnostic accuracy.

5. Conclusion

Direct spectral subtraction increased the paired SNR index in every evaluated lumbar structure and improved blinded visual grading for the spinal cord, degenerated nucleus pulposus, spinal canal, and intervertebral disc on factor-3 GRAPPA 3T sagittal T2-weighted MRI. Interobserver agreement increased from $\kappa = 0.60$ to $\kappa = 0.72$. The mismatch between the large vertebral-body SNR gain and its nonsignificant visual change demonstrates that quantitative improvement must be interpreted in relation to the anatomical task. The principal contribution is a transparent, low-complexity computational workflow that can support diagnostic visibility while retaining the approximately 37% scan-time reduction of factor 3 relative to factor 2.

The results should be validated in larger, prospectively collected, multicenter datasets that retain complete demographics and standardized ROI definitions. Future work should compare direct SSD with spatially adaptive spectral subtraction, nonlocal denoising, compressed sensing, and deep learning reconstruction; report computational cost; examine other MRI sequences and anatomical regions; and evaluate diagnostic accuracy against an independent clinical reference standard.

Acknowledgment

The authors thank the radiology staff and consultant radiologists at RSUD Dr. Soedono Madiun for supporting image acquisition and observer evaluation. The authors also acknowledge the institutional support associated with the original research.

References

[1] N. N. Knezevic, K. D. Candido, J. W. S. Vlaeyen, J. Van Zundert, and S. P. Cohen, "Low back pain," Lancet, vol. 398, no. 10294, pp. 78–92, 2021, doi: 10.1016/S0140-6736(21)00733-9.

[2] J. Hartvigsen et al., "What low back pain is and why we need to pay attention," Lancet, vol. 391, no. 10137, pp. 2356–2367, 2018, doi: 10.1016/S0140-6736(18)30480-X.

[3] Expert Panel on Neurological Imaging et al., "ACR Appropriateness Criteria® Low Back Pain: 2021 Update," J. Am. Coll. Radiol., vol. 18, no. 11S, pp. S361–S379, 2021, doi: 10.1016/j.jacr.2021.08.002.

[4] D. F. Fardon et al., "Lumbar disc nomenclature: Version 2.0," Spine J., vol. 14, no. 11, pp. 2525–2545, 2014, doi: 10.1016/j.spinee.2014.04.022.

[5] C. W. A. Pfirrmann, A. Metzdorf, M. Zanetti, J. Hodler, and N. Boos, "Magnetic resonance classification of lumbar intervertebral disc degeneration," Spine, vol. 26, no. 17, pp. 1873–1878, 2001, doi: 10.1097/00007632-200109010-00011.

[6] W. Brinjikji et al., "Systematic literature review of imaging features of spinal degeneration in asymptomatic populations," AJNR Am. J. Neuroradiol., vol. 36, no. 4, pp. 811–816, 2015, doi: 10.3174/ajnr.A4173.

[7] M. A. Griswold et al., "Generalized autocalibrating partially parallel acquisitions (GRAPPA)," Magn. Reson. Med., vol. 47, no. 6, pp. 1202–1210, 2002, doi: 10.1002/mrm.10171.

[8] K. P. Pruessmann, M. Weiger, M. B. Scheidegger, and P. Boesiger, "SENSE: Sensitivity encoding for fast MRI," Magn. Reson. Med., vol. 42, no. 5, pp. 952–962, 1999, doi: 10.1002/(SICI)1522-2594(199911)42:5<952::AID-MRM16>3.0.CO;2-S.

[9] A. Deshmane, V. Gulani, M. A. Griswold, and N. Seiberlich, "Parallel MR imaging," J. Magn. Reson. Imaging, vol. 36, no. 1, pp. 55–72, 2012, doi: 10.1002/jmri.23639.

[10] P. M. Robson et al., "Comprehensive quantification of signal-to-noise ratio and g-factor for image-based and k-space-based parallel imaging reconstructions," Magn. Reson. Med., vol. 60, no. 4, pp. 895–907, 2008, doi: 10.1002/mrm.21728.

[11] I. Nölte, L. Gerigk, M. A. Brockmann, A. Kemmling, and C. Groden, "MRI of degenerative lumbar spine disease: Comparison of non-accelerated and parallel imaging," Neuroradiology, vol. 50, no. 5, pp. 403–409, 2008, doi: 10.1007/s00234-008-0363-0.

[12] J. Fruehwald-Pallamar et al., "Parallel imaging of the cervical spine at 3T: Optimized trade-off between speed and image quality," AJNR Am. J. Neuroradiol., vol. 33, no. 10, pp. 1867–1874, 2012, doi: 10.3174/ajnr.A3101.

[13] G. Bratke et al., "Accelerated MRI of the lumbar spine using compressed sensing: Quality and efficiency," J. Magn. Reson. Imaging, vol. 49, no. 7, pp. e164–e175, 2019, doi: 10.1002/jmri.26526.

[14] S. Aja-Fernández, C. Alberola-López, and C.-F. Westin, "Noise and signal estimation in magnitude MRI and Rician distributed images: A LMMSE approach," IEEE Trans. Image Process., vol. 17, no. 8, pp. 1383–1398, 2008, doi: 10.1109/TIP.2008.925382.

[15] H. Gudbjartsson and S. Patz, "The Rician distribution of noisy MRI data," Magn. Reson. Med., vol. 34, no. 6, pp. 910–914, 1995, doi: 10.1002/mrm.1910340618.

[16] M. A. Ertürk, P. A. Bottomley, and A. M. M. El-Sharkawy, "Denoising MRI using spectral subtraction," IEEE Trans. Biomed. Eng., vol. 60, no. 6, pp. 1556–1562, 2013, doi: 10.1109/TBME.2013.2239293.

[17] I. Maulidya, Fatimah, and G. Santoso, "Application of spectral subtraction denoising on 3 T MRI in lumbar spine (herniated nucleus pulposus case) GRAPPA to improve CNR," J. Phys.: Conf. Ser., vol. 1943, art. 012049, 2021, doi: 10.1088/1742-6596/1943/1/012049.

[18] J. V. Manjón, P. Coupé, L. Martí-Bonmatí, D. L. Collins, and M. Robles, "Adaptive non-local means denoising of MR images with spatially varying noise levels," J. Magn. Reson. Imaging, vol. 31, no. 1, pp. 192–203, 2010, doi: 10.1002/jmri.22003.

[19] J. Veraart, D. S. Novikov, D. Christiaens, B. Ades-Aron, J. Sijbers, and E. Fieremans, "Denoising of diffusion MRI using random matrix theory," NeuroImage, vol. 142, pp. 394–406, 2016, doi: 10.1016/j.neuroimage.2016.08.016.

[20] H. Yoo et al., "Deep learning-based reconstruction for acceleration of lumbar spine MRI: A prospective comparison with standard MRI," Eur. Radiol., vol. 33, pp. 8656–8668, 2023, doi: 10.1007/s00330-023-09918-0.

[21] H. Tang et al., "Deep learning reconstruction for lumbar spine MRI acceleration: A prospective study," Eur. Radiol. Exp., vol. 8, art. 67, 2024, doi: 10.1186/s41747-024-00470-0.

[22] M. Han et al., "Qualitative and quantitative analysis of accelerated lumbar spine MRI with deep-learning based image reconstruction at 3T," Pain Med., vol. 24, suppl. 1, pp. S149–S159, 2023, doi: 10.1093/pm/pnad035.

[23] M. Fujiwara et al., "Ultrafast lumbar spine MRI protocol using deep learning-based reconstruction: Diagnostic equivalence to a conventional protocol," Skeletal Radiol., vol. 52, no. 2, pp. 233–241, 2023, doi: 10.1007/s00256-022-04192-5.

[24] N. Kashiwagi et al., "Applicability of deep learning-based reconstruction trained by brain and knee 3T MRI to lumbar 1.5T MRI," Acta Radiol. Open, vol. 10, no. 6, 2021, doi: 10.1177/20584601211023939.

[25] S. Sun et al., "Evaluation of deep learning reconstructed high-resolution 3D lumbar spine MRI," Eur. Radiol., vol. 32, pp. 6167–6177, 2022, doi: 10.1007/s00330-022-08708-4.

[26] H. Almansour et al., "Deep learning reconstruction for accelerated spine MRI: Prospective analysis of interchangeability," Radiology, vol. 306, art. e212922, 2023, doi: 10.1148/radiol.212922.

[27] K. Yasaka et al., "Deep learning reconstruction for 1.5 T cervical spine MRI: Effect on interobserver agreement in the evaluation of degenerative changes," Eur. Radiol., vol. 32, pp. 6118–6125, 2022, doi: 10.1007/s00330-022-08729-z.

[28] K. Yasaka et al., "Super-resolution deep learning reconstruction to evaluate lumbar spinal stenosis status on magnetic resonance myelography," Jpn. J. Radiol., vol. 43, pp. 1427–1433, 2025, doi: 10.1007/s11604-025-01787-5.

[29] C. Montin et al., "Seeking a widely adoptable practical standard to estimate signal-to-noise ratio in magnetic resonance imaging for multiple-coil reconstructions," J. Magn. Reson. Imaging, vol. 54, no. 6, pp. 1952–1964, 2021, doi: 10.1002/jmri.27816.

[30] M. Båth and L. G. Månsson, "Visual grading characteristics analysis: A non-parametric rank-invariant statistical method for image quality evaluation," Br. J. Radiol., vol. 80, no. 951, pp. 169–176, 2007, doi: 10.1259/bjr/35012658.

[31] J. R. Landis and G. G. Koch, "The measurement of observer agreement for categorical data," Biometrics, vol. 33, no. 1, pp. 159–174, 1977, doi: 10.2307/2529310.

[32] M. L. McHugh, "Interrater reliability: The kappa statistic," Biochem. Med., vol. 22, no. 3, pp. 276–282, 2012, doi: 10.11613/BM.2012.031.

[33] F. Knoll et al., "fastMRI: A publicly available raw k-space and DICOM dataset of knee images for accelerated MR image reconstruction using machine learning," Radiol. Artif. Intell., vol. 2, no. 1, art. e190007, 2020, doi: 10.1148/ryai.2020190007.

[34] M. J. Muckley et al., "Results of the 2020 fastMRI challenge for machine learning MR image reconstruction," IEEE Trans. Med. Imaging, vol. 40, no. 9, pp. 2306–2317, 2021, doi: 10.1109/TMI.2021.3075856.

[35] K. Hammernik et al., "Learning a variational network for reconstruction of accelerated MRI data," Magn. Reson. Med., vol. 79, no. 6, pp. 3055–3071, 2018, doi: 10.1002/mrm.26977.

[36] H. K. Aggarwal, M. P. Mani, and M. Jacob, "MoDL: Model-based deep learning architecture for inverse problems," IEEE Trans. Med. Imaging, vol. 38, no. 2, pp. 394–405, 2019, doi: 10.1109/TMI.2018.2865356.